Monthly Notices of the ROYAL ASTRONOMICAL SOCIETY

MNRAS **504,** 769–781 (2021)
Advance Access publication 2021 March 31

doi:10.1093/mnras/stab769

Clustering and halo abundances in early dark energy cosmological models

Anatoly Klypin,[1,2]★ Vivian Poulin,[3] Francisco Prada,[4] Joel Primack,[5] Marc Kamionkowski,[6] Vladimir Avila-Reese,[7] Aldo Rodriguez-Puebla,[7] Peter Behroozi,[8] Doug Hellinger[5] and Tristan L. Smith[9]

[1]*Department of Astronomy, New Mexico State University, Las Cruces, 88003 NM, USA*
[2]*Department of Astronomy, University of Virginia, Charlettesville, 22904 VA, USA*
[3]*Laboratoire Univers & Particules de Montpellier, CNRS & Universite de Montpellier, Montpelier, 34090, France*
[4]*Instituto de Astrofísica de Andalucía (CSIC), Glorieta de la Astronomía, E-18080 Granada, Spain*
[5]*Department of Physics and SCIPP, University of California, Santa Cruz, CA 95064, USA*
[6]*Department of Physics and Astronomy, Johns Hopkins University, Baltimore, MD 21218, USA*
[7]*Instituto de Astronomía, Universidad Nacional Autónoma de México, A.P. 70-264, 04510 CDMX, Mexico*
[8]*Steward Observatory, University of Arizona, Tucson, 85719 AZ, USA*
[9]*Department of Physics and Astronomy, Swarthmore College, 500 College Ave., Swarthmore, PA 19081, USA*

Accepted 2021 March 8. Received 2021 March 2; in original form 2020 August 5

ABSTRACT

Cold Dark Matter with cosmological constant (ΛCDM) cosmological models with early dark energy (EDE) have been proposed to resolve tensions between the Hubble constant $H_0 = 100\,h\,\mathrm{km\,s^{-1}\,Mpc^{-1}}$ measured locally, giving $h \approx 0.73$, and H_0 deduced from *Planck* cosmic microwave background (CMB) and other early-Universe measurements plus ΛCDM, giving $h \approx 0.67$. EDE models do this by adding a scalar field that temporarily adds dark energy equal to about 10 per cent of the cosmological energy density at the end of the radiation-dominated era at redshift $z \sim 3500$. Here, we compare linear and non-linear predictions of a *Planck*-normalized ΛCDM model including EDE giving $h = 0.728$ with those of standard *Planck*-normalized ΛCDM with $h = 0.678$. We find that non-linear evolution reduces the differences between power spectra of fluctuations at low redshifts. As a result, at $z = 0$ the halo mass functions on galactic scales are nearly the same, with differences only 1–2 per cent. However, the differences dramatically increase at high redshifts. The EDE model predicts 50 per cent more massive clusters at $z = 1$ and twice more galaxy-mass haloes at $z = 4$. Even greater increases in abundances of galaxy-mass haloes at higher redshifts may make it easier to reionize the universe with EDE. Predicted galaxy abundances and clustering will soon be tested by the *James Webb Space Telescope* (*JWST*) observations. Positions of baryonic acoustic oscillations (BAOs) and correlation functions differ by about 2 per cent between the models – an effect that is not washed out by non-linearities. Both standard ΛCDM and the EDE model studied here agree well with presently available acoustic-scale observations, but the Dark Energy Spectroscopic Instrument and *Euclid* measurements will provide stringent new tests.

Key words: large-scale structure of Universe – dark matter – galaxies: haloes – methods: numerical.

1 INTRODUCTION

Combined late-universe measurements give the value of the Hubble constant $h = 0.733 \pm 0.008$ according to a recent review of Verde, Treu & Riess (2019). This value of the expansion rate is in as much as 6σ conflict with the value $h = 0.674 \pm 0.005$ from the *Planck* measurements of the cosmic microwave background (CMB) temperature and polarization and other early-universe observations extrapolated to the present epoch using standard ΛCDM (Planck Collaboration VI 2018). This discrepancy is unlikely to be a statistical fluke, and it is not easily attributable to any systematic errors (e.g. Freedman 2017; Riess et al. 2019; Aylor et al. 2019). Instead, it may be telling us that there is a missing ingredient in standard ΛCDM. Of the many potential explanations that have been proposed, a brief episode of early dark energy (EDE) around the time of matter dominance followed by ΛCDM evolution (Poulin et al. 2019; Knox & Millea 2020; Smith, Poulin & Amin 2020; Agrawal et al. 2019; Lin et al. 2019) has received perhaps the most attention. For the model we consider here, Poulin et al. (2019) and Smith et al. (2020, SPA20) have shown that their fluctuating scalar field EDE model can fit all the CMB data as well as the usual standard 6-parameter ΛCDM does, and also give H_0 in agreement with the recent local-universe measurements. As Fig. 1 shows, in this model the EDE contributes a maximum of only about 10 per cent to the total cosmic density at redshifts $z \sim 3500$, at the end of the era of radiation domination and the beginning of matter domination.

The resulting best-fitting cosmic parameters (see Table 1) are interestingly different from those of standard ΛCDM. In particular, both the primordial power spectrum amplitude A_s and σ_8, measuring the linear amplitude today at $8\,h^{-1}$ Mpc, are larger than for the latest *Planck* analysis with standard ΛCDM. Also, n_s, the slope of the

★ E-mail: aklypin@nmsu.edu

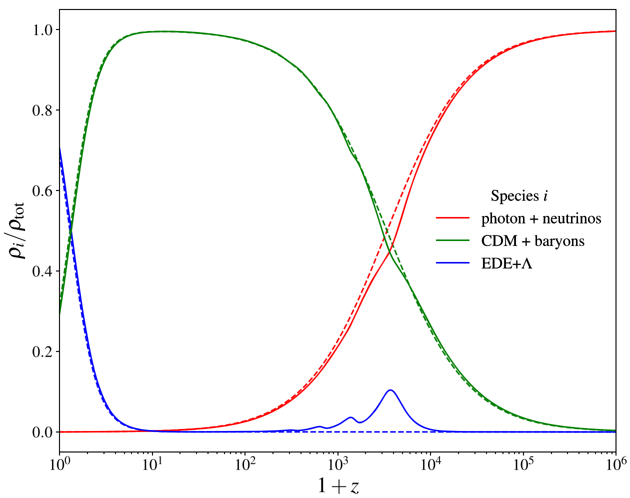

Figure 1. Densities of different components at different redshifts for EDE (the full curves) and the standard ΛCDM model (the dashed curves). Oscillating early dark energy density (the blue curve) peaks at $z \sim 3500$ when it contributes ∼ 10 per cent to the total density. Its contribution quickly decreases after that.

Table 1. Parameters of cosmological models.

Parameter	EDE SPA20	ΛCDM MultiDark-*Planck*13	ΛCDM CMB-*Planck*18
$\Omega_{\rm m}$	0.293	0.307	0.315 ± 0.007
$\Omega_{\rm cold}h^2$	0.132	0.119	0.120 ± 0.001
$\Omega_{\rm bar}h^2$	0.0225	0.0221	0.0224 ± 0.0001
H_0 (km s^{-1} Mpc^{-1})	72.81	67.77	67.36 ± 0.54
$n_{\rm s}$	0.986	0.965	0.965 ± 0.004
σ_8	0.836	0.820	0.811 ± 0.006
Age (Gyr)	13.032	13.825	13.797 ± 0.023
$z_{\rm drag}$	1061.28	1059.09	1059.94 ± 0.30
$r_{\rm drag}$ (Mpc)	140.1	147.8	147.1 ± 0.3

power primordial power spectrum is larger than for standard ΛCDM. And with the higher H_0, the present age of the universe is 13.0 Gyr rather than 13.8 Gyr. Such modifications of the cosmological parameters are also produced in other recent papers on EDE (Agrawal et al. 2019; Lin et al. 2019).

Particle theory provides many scalar fields that could have non-zero potential energy temporarily preserved by Hubble friction, leading to temporary episodes of effective dark energy (e.g. Dodelson, Kaplinghat & Stewart 2000; Griest 2002; Kamionkowski, Pradler & Walker 2014). It has long been known that dark energy contributions at early cosmic times can imply modifications of CMB, big-bang nucleosynthesis, and large-scale structure formation (Doran et al. 2001; Müller, Schäfer & Wetterich 2004; Bartelmann, Doran & Wetterich 2006).

Only recently has resolving the Hubble tension become a motivation for EDE (Karwal & Kamionkowski 2016; Poulin et al. 2019). The challenge lies in finding ways in which the Hubble parameter inferred from the CMB can be made larger without introducing new tensions with the detailed CMB peak structure and/or other well-established cosmological constraints. In particular, all solutions are constrained by the remarkable precision (roughly one part in 10^4) with which the angular scale $\theta_{\rm a}$ of the acoustic peaks in the CMB power spectrum is fixed. Roughly speaking, this angular scale is set by $\theta_{\rm a} \propto r_{\rm s}/D_{\rm A}$, where $r_{\rm s}$ is the comoving sound horizon at the surface of last scatter and $D_{\rm A}$ is the comoving distance to the surface of last scatter.

There are two possibilities to keep $\theta_{\rm a}$ fixed: keep $D_{\rm A}$ fixed by compensating the increase of energy today (H_0 higher means higher energy density today) by decreasing the energy density at earlier times through a change to the late-time expansion history, or decreasing $r_{\rm s}$ by the same amount as $D_{\rm A}$ through a change to the early-time physics. However, modifications to the late-time expansion history are constrained by measurements of baryonic acoustic oscillations (BAOs) and luminosity distance to supernovae, and early-time solutions are constrained by the detailed structure of the higher acoustic peaks in the CMB power spectra (Bernal, Verde & Riess 2016). Even so, Poulin et al. (2018) and subsequent studies (Agrawal et al. 2019; Lin et al. 2019; Poulin et al. 2019; Smith et al. 2020) were able to find regions of the parameter space of EDE models that provide a good fit to the data. Still, more work must be done – both in terms of theory and new measurements – to assess the nature of viable EDE models.

We have chosen to focus on the Smith et al. (2020) version of EDE because it was engineered to fit the details of the high-l CMB polarization data, and because it represents the best fit to the local H_0 measurements and the largest deviation of the cosmological parameters from standard ΛCDM, which should lead to the clearest differences in testable predictions. These new cosmological models will make specific predictions for galaxy mass and luminosity functions and galaxy clustering. Given that these phenomena arise from non-linear evolution of primordial perturbations and involve gas dynamics, the power of numerical simulations is essential. Of course, it is possible that the result of such observational tests of EDE will be to eliminate this class of cosmological models. But if not, EDE potentially tells us about a phenomenon that contributes to early cosmic evolution, and about another scalar field important in the early universe besides the putative inflaton responsible for the cosmic inflation that set the stage for the big bang.

The key features that distinguish EDE from LCDM (smaller sound horizon, higher $\Omega_{\rm cdm}h^2$, higher $n_{\rm s}$) are shared by all types of EDE model suggested to resolve the Hubble tension, and even by many other 'early-universe' solutions. Unless additional 'interactions' are added, the naive requirement of an increase in $H(z)$ at $z \gtrsim 1000$ will necessarily require such shifts in these cosmological parameters to compensate the early integrated Sachs–Wolfe effect in the CMB (Poulin et al. 2019; Hill et al. 2020), as well as keeping the BAO scale fixed at late times (Jedamzik, Pogosian & Zhao 2020). The model we study here is thus a well-motivated proxy for testing a broad category of solutions to the Hubble tension.

There were some earlier efforts to study effects of non-linear evolution in models called EDE (Bartelmann et al. 2006; Francis, Lewis & Linder 2009; Grossi & Springel 2009; Fontanot et al. 2012). However, models for the dark energy used in those papers are very different compared with those discussed in this paper. As a matter of fact, there is little in common – with the exception of the name EDE – between those models and the model we consider here. The equation of state w of dark energy $P = w\rho c^2$ in those papers is $w = -1$ only at $z = 0$ and has significant deviations from $w = -1$ at low redshifts. For example, models used by Grossi & Springel (2009) and Fontanot et al. (2012) had $w = -0.7$ at $z = 1$ and $w = -0.4$ at $z = 5$. This should be compared with $w = -1$ at $z \lesssim 1000$ in our EDE model.

In the sense of dynamics of growth of fluctuations in the matter-dominated era in our EDE model, we are dealing with a vanilla ΛCDM model with the only modification being the spectrum of fluctuations. Even the spectrum of fluctuations is not much different:

a 2 per cent change in σ_8 and 0.02 difference in the slope of the spectrum. With these small deviations, one might imagine that the final non-linear statistics (such as power, correlation functions, halo mass functions) would be very similar. But instead we find very significant differences, especially at redshifts $z > 1$.

The S_8 tension is the conflict between weak lensing and other local observations that imply a relatively low value of $S_8 \equiv \sigma_8\sqrt{\Omega_m/0.3}$ and the higher value of S_8 of both the *Planck*-normalized ΛCDM and the EDE model considered here (Smith et al. 2020). Our EDE model has $\sigma_8 = 0.836$, larger than $\sigma_8 = 0.820$ of our fiducial *Planck* 2013 MultiDark model or the *Planck* 2018 value $\sigma_8 = 0.811 \pm 0.006$. But what is determined by CMB observations is $\Omega_m h^2$, and the higher value of H_0 with EDE means that the resulting $S_8 = 0.830$ is identical to that from *Planck* 2018 (Combined value, table 1 of Planck Collaboration VI 2018).

The latest weak lensing measurements of S_8 are the Dark Energy Survey year 1 (DES-Y1) cosmic shear results $S_8 = 0.782^{+0.027}_{-0.027}$ (Troxel et al. 2018); the Hyper Suprime-Cam Year 1 (HSC-Y1) cosmic shear power spectra, giving $S_8 = 0.800^{+0.029}_{-0.028}$ (Hikage et al. 2019); and the HSC-Y1 cosmic shear two-point correlation functions, giving $S_8 = 0.804^{+0.032}_{-0.029}$ (Hamana et al. 2020). These measurements are all in less than 2σ disagreement with $S_8 = 0.830$ from *Planck*-normalized ΛCDM and our EDE model. Hill et al. (2020) claim that the EDE model considered here, and other EDE models, are in serious tension with large-scale structure measurements. They cite the DES-Y1 result $S_8 = 0.773^{+0.026}_{-0.020}$, obtained by combining weak lensing with galaxy clustering (Abbott et al. 2019), which disagrees by 2.3σ with $S_8 = 0.830$. However, Abbott et al. (2019) allowed the total neutrino mass free to vary, which leads to a somewhat lower DES-inferred S_8 than that, $S_8 = 0.792 \pm 0.024$, which arises if $\sum m_\nu = 0.06$ eV is fixed, as the *Planck* team (Planck Collaboration VI 2018) and we have done. Similarly, the shear-only result was analysed by the SPTPol collaboration with the same convention as ours. They obtained $S_8 = 0.79^{+0.4}_{-0.029}$ (Bianchini et al. 2020), to be compared with $S_8 = 0.782 \pm 0.027$ once the sum of neutrino masses is left free to vary (Troxel et al. 2018). While there is indeed some S_8 tension between the DES-Y1 measurements and the prediction of our EDE model, it remains true that the addition of a brief period of EDE resolves the ΛCDM Hubble tension and fits the *Planck* 2018 CMB observations without exacerbating the S_8 tension. This is confirmed from table 7 of Hill et al. (2020), where one can read off that the joint DES-Y1 χ^2 goes from 506.4 for ΛCDM to 507.7 for the EDE cosmology, a marginal degradation given that the joint DES-Y1 data have 457 data points (Abbott et al. 2019). This allows us to conclude that the DES-Y1 result does not exclude the presence of EDE.

This was also demonstrated by Murgia, Abellán & Poulin (2020), where MCMC analyses of the EDE model against KiDS and DES data were performed (see also Chudaykin, Gorbunov & Nedelko (2020) for an analysis based on SPTPol data reaching similar conclusions). Additionally, it was recently suggested that the ‘Effective Field Theory’ analysis of BOSS data excludes the EDE solution due to the additional constraints on the CDM density $\omega_{\rm cdm}$ it provides (D’Amico et al. 2020; Ivanov et al. 2020). However, Smith et al. (2020) show that the ‘constraint’ comes from a small ($\sim 2\sigma$) tension in the reconstruction of the primordial power spectrum amplitude A_s between BOSS and *Planck*. Nevertheless, it was also shown that EDE can reach a H_0 value as high as 71 km s^{-1} Mpc^{-1} and provide a fit as good as the ΛCDM one. Therefore, further measurements by DES, HSC, and other programs will be important tests for cosmological models as they improve the precision of measurements of S_8 and other cosmological parameters.

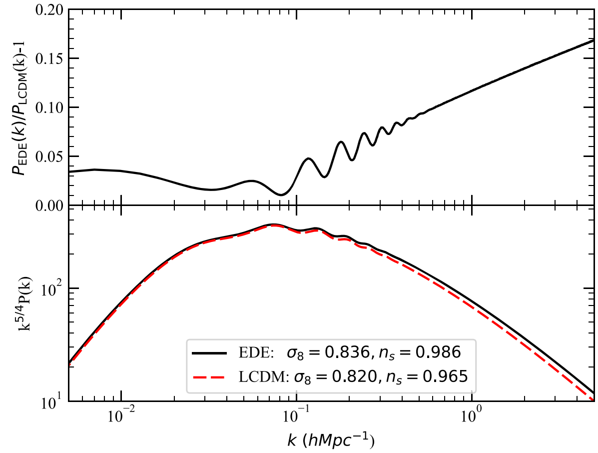

Figure 2. *Bottom panel:* Linear power spectrum of dark matter fluctuations at $z = 0$ scaled with factor $k^{5/4}$ to reduce the dynamical range and to make the domain of BAOs $k = (0.07 - 0.3)h$Mpc^{-1} more visible. *Top panel:* The ratio of power spectra in our EDE model to that of the standard ΛCDM model. The amplitude of fluctuations in our EDE model is always larger than in ΛCDM though the differences at long wavelengths $\lesssim 0.1\,h$ Mpc^{-1} are only (2–3) per cent. The differences increase at large k and become substantial ($\sim$ 20 per cent) on galactic scales $k \gtrsim 5h$Mpc^{-1}.

In this paper, we compare for the first time the predictions for large-scale structure observables between standard ΛCDM and EDE. Through a suite of non-linear simulations, we compute the halo mass function and the BAOs (and correlation functions) at various redshifts. We find significant differences that will allow future observations such as those from ROentgen Survey with an Imaging Telescope Array (eROSITA; Merloni et al. 2012), James Webb Space Telescope (*JWST*),[1] Dark Energy Spectroscopic Instrument (DESI),[2] and *Euclid* space mission[3] to critically test such cosmologies.

We use extensive *N*-body simulations to study the effects of non-linear evolution. As a benchmark, we employ a ΛCDM model with the parameters and spectrum of the MultiDark-*Planck* simulations (Klypin et al. 2016; Rodríguez-Puebla et al. 2016). Table 1 lists those parameters and Fig. 2 compares linear power spectra. MultiDark-*Planck* is a well-studied ΛCDM model based on the 2013 *Planck* cosmological parameters (Planck Collaboration XVI 2014) that has been used in many publications. Sophisticated analyses of galaxy statistics applied to different MultiDark-*Planck* numerical simulations show that the model reproduces the observed clustering of galaxies in samples such as SDSS and BOSS (e.g. Guo et al. 2015; Kitaura et al. 2016; Rodríguez-Torres et al. 2016). Analyses of this kind – matching selection functions, boundaries of observational sample, light cones, and stellar luminosity functions – are difficult to implement and require high-resolution simulations. We plan to do such simulations in the future for the EDE model considered here, but for now we are interested in learning what differences to expect and what statistics should be promising to distinguish between standard ΛCDM models compared with with EDE ones.

In Section 2, we describe the cosmological simulations used in this paper, and in Section 3 we present and discuss the resulting power spectra. In Section 4, we compare the baryon acoustic oscillations and corresponding correlation functions between ΛCDM and the EDE

[1] *James Webb Space Telescope*; https://www.jwst.nasa.gov/.
[2] Dark Energy Spectroscopic Instrument; https://www.desi.lbl.gov/.
[3] https://www.Euclid-ec.org/

Table 2. Numerical and cosmological parameters of different simulations. The columns give the simulation identifier, cosmology, the size of the simulated box in h^{-1} Mpc, the number of particles, the mass per simulation particle $m_{\rm p}$ in units of $h^{-1}\,{\rm M}_{\odot}$, the mesh size $N_{\rm g}{}^3$, the comoving gravitational softening length Δx in units of h^{-1} Mpc, the number of time-steps $N_{\rm step}$, initial redshift, and the number of realizations $N_{\rm r}$. Additional smaller scale simulations are discussed in Section 6.

Simulation	Cosmology	Box	Particles	$m_{\rm p}$	$N_{\rm g}{}^3$	Δx	$N_{\rm s}$	$z_{\rm init}$	$N_{\rm r}$
$\mathrm{EDE}_{0.5}$	EDE	500^3	2000^3	1.3×10^9	7000^3	0.071	253	150	5
EDE_{1}	EDE	1000^3	2000^3	1.0×10^{10}	7000^3	0.143	136	100	16
EDE_{2A}	EDE	2000^3	2000^3	8.3×10^{10}	7000^3	0.285	130	150	6
EDE_{2B}	EDE	2000^3	2000^3	8.3×10^{10}	4000^3	0.500	130	150	210
$\Lambda\mathrm{CDM}_{0.5}$	MultiDark	500^3	2000^3	1.3×10^9	7000^3	0.071	253	150	5
$\Lambda\mathrm{CDM}_{1}$	MultiDark	1000^3	2000^3	1.1×10^{10}	7000^3	0.143	136	100	30
$\Lambda\mathrm{CDM}_{2A}$	MultiDark	2000^3	2000^3	8.3×10^{10}	7000^3	0.285	130	100	15
$\Lambda\mathrm{CDM}_{2B}$	MultiDark	2000^3	2000^3	8.3×10^{10}	4000^3	0.500	130	150	210

model. In Section 5, we discuss the changes in halo abundances in EDE out to redshift $z = 4$, and explain the origin of these changes. In Section 6, we discuss halo abundance and clustering at even higher redshifts, including implications for reionization of the universe. Section 7 is a summary and discussion of our results.

2 SIMULATIONS

Most of the results presented in this paper are based on new cosmological N-body simulations. The simulations were carried out with the parallel particle-mesh code GLAM (Klypin & Prada 2018). Because the GLAM code is very fast, we have done many realizations of the simulations with the same cosmological and numerical parameters that only differ by the initial random seed. A large number of realizations is quite important because the differences between EDE and ΛCDM models are not very large. This is especially true on long wavelengths $k \lesssim 0.1\,h$ Mpc^{-1} where the difference in the power spectra is just ~2 per cent. So, one needs many realizations to reduce the cosmic variance and see the real differences.

All the GLAM simulations were started at initial redshift $z_{\rm init} = 100$ or $z_{\rm init} = 150$ using the Zeldovich approximation. Table 2 presents the numerical parameters of our simulation suite: box size, number of particles, particle mass $m_{\rm p}$, number of mesh points N_g^3, cell size of the density/force mesh Δx, the number of time-steps $N_{\rm step}$, and the number of realizations $N_{\rm r}$.

The GLAM code is very fast compared with high-resolution codes such as GADGET (Springel 2005) or ART (Kravtsov, Klypin & Khokhlov 1997). For example, our most expensive simulations $\mathrm{EDE}_{0.5}$ and $\Lambda\mathrm{CDM}_{0.5}$ used just ~2500 cpu-h on a dual Intel Platinum 8280M computational node, which is just 2 d of wall-clock time. The limiting factor of GLAM simulations is the force resolution Δx. It is defined by the cell size – the ratio of the comoving box size L to the mesh size $N_{\rm g}$: $\Delta x = L/N_{\rm g}$. So, the larger the mesh size $N_{\rm g}$, the better is the resolution. Klypin & Prada (2018) give detailed analysis of convergence and accuracy of the GLAM code. Additional tests are presented in the Appendix where we compare GLAM results for the power spectrum and halo mass function with high-resolution Quijote (Villaescusa-Navarro et al. 2020) and Uchuu (Ishiyama et al. 2020) simulations.

Just as with any particle-mesh code, the resolution is defined by the available memory: the larger the memory, the better the resolution. We use computational nodes each with 1.5Tb RAM and two Intel Platinum 8280M processors with combined 56 cores.

We use a spherical overdensity (SO) halo finder, which is a stripped down variant of the bound density maxima (BDM) halo finder (Klypin, Trujillo-Gomez & Primack 2011; Knebe et al. 2011). Limited force resolution does not allow subhaloes to survive in virialized haloes. This is why we study only distinct haloes (those that are not subhaloes) in this paper.

3 POWER SPECTRA

Fig. 2 shows the $z = 0$ linear power spectra of fluctuations in the EDE and ΛCDM models. Differences between power spectra of fluctuations are relatively small. On long wavelengths ($k \lesssim 0.1\,h$ Mpc^{-1}), the differences are mostly explained by the normalizations: $[\sigma_8(EDE)/\sigma_8(\Lambda\mathrm{CDM})]^2 = 1.039$. The differences increase on small scales and become substantial. For example, at $k = 5\,h$ Mpc^{-1} the amplitude of fluctuations in the EDE model is 17 per cent bigger than in the ΛCDM model.

The reason for this increase comes from the differences in the slope $n_{\rm s}$ of the primordial power spectra. At first sight, the difference of 0.02 in the slope seems to be small. However, it results in large differences in amplitude when one compares waves that differ dramatically in wavelength: 15 per cent for waves that differ by a factor of 1000 in wavelength. A more subtle effect is related to the halo mass function, which depends not only on the amplitude of fluctuations but also on the slope of the power spectrum.

The domain of BAOs ($k = 0.07$–$0.3\,h$ Mpc^{-1}) is also different in the models. At first glance, the wiggles that are clearly seen in the top panel of Fig. 2 are the familiar BAOs. They are not, though they are related to BAOs. If the positions of the BAO peaks were the same, there would not have been wiggles in the ratio of the power spectra. Without the EDE component the position of BAO peaks is mostly defined by $\Omega_{\rm bar}/\Omega_{\rm m}$ and $\Omega_{\rm m}h^2$ (Eisenstein & Hu 1998). There is an additional effect in EDE models due to the fact that the EDE changes the dynamics of acoustic waves before the recombination. So, the very presence of the wiggles tells us that BAO peaks happen at different wavenumbers: in the EDE models the BAOs are shifted to slightly smaller wavenumbers.

Non-linear evolution modifies the power spectra. Fig. 3 shows results of our simulations at redshift $z = 0$. Results from different box sizes and resolutions nicely match each other in overlapping regions. As the result, we stack together different simulations and extend the range of resolved scales.

As clearly seen in Fig. 3 the non-linear evolution dramatically changes the shape of the power spectrum: at $k \gtrsim 0.5\,h$ Mpc^{-1} the fluctuations are much larger compared with the linear regime. The bump at $k \sim 1.5\,h$ Mpc^{-1} corresponds to mass $M = (4\pi/3)\Omega_m\rho_{\rm cr}(\lambda/2)^3 \approx 10^{13}\,h^{-1}\,{\rm M}_{\odot}$ – scale of large galaxies like

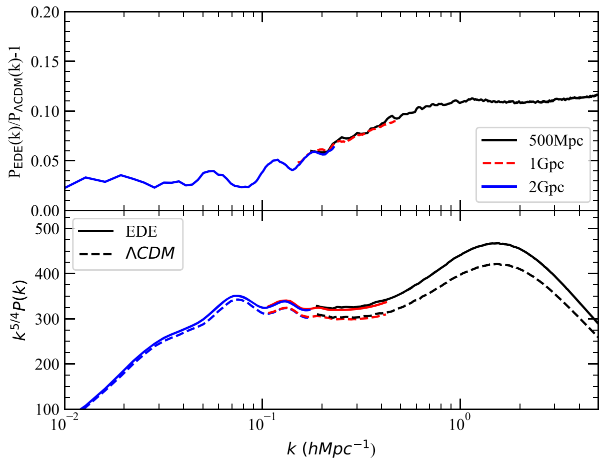

Figure 3. Similar to Fig. 2 but for non-linear evolution at $z = 0$. Results from different box sizes and resolutions nicely match in overlapping regions. Non-linear evolution dramatically changes the shape of the power spectrum at small scales. The BAO peaks are slightly damped, broadened, and shifted. To some degree the non-linear effects reduce the differences between the models, but they do not wipe them out.

our Milky Way. So, the bump is a manifestation of collapsing dark matter haloes.[4]

To some degree the non-linear effects reduce the differences between the models at strongly non-linear regime $k \gtrsim 1\,h$ Mpc^{-1}. Here, the ratios of the power spectra are nearly constant 10 per cent – a marked deviation from the linear spectra shown in Fig. 2. This nearly constant ratio of non-linear spectra produces small and hardly detectable differences in the abundance of haloes at $z = 0$. Note that at larger redshifts the differences are larger than at $z = 0$ because the non-linearities are smaller.

The power spectra in the domain of BAOs are also affected by non-linearites, but in a more subtle way. The BAO peaks are slightly damped, broadened, and shifted: effects that are well understood and well studied (e.g. Eisenstein, Seo & White 2007; Angulo et al. 2008; Prada et al. 2016), see Section 4 for a detailed study. At even larger scales $k \lesssim 0.05\,h$ Mpc^{-1}, the fluctuations are still in the nearly linear regime.

The fact that non-linear evolution reduces differences between EDE and ΛCDM models is a welcome feature. We know that at low redshifts $z \lesssim 0.5$ the ΛCDM model reproduces the observed clustering of galaxies in samples such as SDSS and BOSS (Guo et al. 2015; Kitaura et al. 2016; Rodríguez-Torres et al. 2016). So, too large deviations from ΛCDM may point to problems. Nevertheless, though relatively small, the deviations still exist and potentially can be detected. The fact that non-linear evolution reduces the differences implies that one also expects larger differences at higher redshifts. Indeed, this is what we find from analysis of halo abundances discussed below.

4 BARYONIC ACOUSTIC OSCILLATIONS

Fig. 4 displays the linear power spectra for the EDE (the solid line) and two ΛCDM models in the domain of the BAO features. In order to appreciate more clearly their overall P(k) shapes and BAO differences, the two ΛCDM models have been normalized to have the same $\sigma_8 = 0.836$ as that of EDE. One ΛCDM model is otherwise the MultiDark-*Planck* one (the dot-solid line). The other ΛCDM model (named ΛCDM_EDE, the dashed line) has the same cosmological parameters as EDE but without the effects of the EDE component.

Compared with ΛCDM, the BAO peaks in the EDE model are systematically shifted. This happens because of a combination of different factors: change of the expansion rate before the recombination, change in the Hubble constant, and in the sound horizon. The sound horizon $r_{\rm d}$ in the EDE cosmology is smaller compared to the ΛCDM_EDE model ($r_{\rm d}$ = 143.92 Mpc) despite both cosmologies having the same cosmological parameters, and hence the BAO peaks in the latter are shifted towards larger scales. In the concordance ΛCDM models, the positions of the acoustic peaks are defined by $\Omega_{\rm m}h^2$ and $\Omega_{\rm bar}h^2$ (see Aubourg et al. 2015). But the propagation of acoustic waves is different in EDE models, as the EDE boosts the Hubble rate around $z_{\rm eq}$ and thus these two cosmological parameters no longer define the BAO peak positions.

The relative difference between the BAO wiggles in the three cosmologies is better seen in Fig. 5, where we show the deviations for each linear power spectrum from that without BAO features obtained from the (Eisenstein & Hu 1998) 'non-wiggle' $P_{\rm nw}$(k) fitting formula. The BAO shifts among the three cosmological models are clearly visible, and systematically shifted towards smaller wavenumbers by 1.8 per cent for EDE and 4.4 per cent for ΛCDM_EDE with respect to the ΛCDM BAO positions. This is expected given their corresponding acoustic sound horizon ratios $r_{\rm d}/r_{\rm d}^{\rm fid}$, where $r_{\rm d}^{\rm fid}$ is the sound horizon of our fiducial cosmology, the ΛCDM model.

The BAO position in the spherically averaged two-point clustering statistics, and hence the acoustic-scale distance measurements obtained from large galaxy redshift surveys, are based on the constraints of the stretch or dilation parameter α defined as

$$\alpha \equiv \frac{(D_{\rm V}(z)/r_{\rm d})}{(D_{\rm V}^{\rm fid}(z)/r_{\rm d}^{\rm fid})}, \qquad (1)$$

where $D_{\rm V}(z) \equiv [cz(1+z)^2 D_{\rm A}^2 H^{-1}(z)]^{1/3}$ is the dilation distance (Eisenstein et al. 2005), $D_{\rm A}$ is the angular diameter distance, and $H(z)$ is the Hubble parameter. The stretch parameter α is measured from the best-fitting model to the observed isotropic power spectrum or correlation function on the scale range $0.05\,h$/Mpc $\lesssim k \lesssim 0.3\,h$/Mpc (see e.g. Anderson et al. 2014; Ross et al. 2015). The latest and more accurate acoustic-scale distance $D_{\rm V}/r_{\rm d}$ measurements, relative to the prediction from *Planck* TT, TE, EE + lowE + lensing (CMB) in the base-ΛCDM model (i.e. our fiducial MultiDark-*Planck*13 cosmology, see Table 1) are shown in Fig. 6. The curves in Fig. 6 correspond to the model predictions from EDE (solid), MultiDark-ΛCDM (dashed), and ΛCDM with the same EDE cosmological parameters (dash–dotted). We conclude that EDE and our ΛCDM cosmology models both agree well with the observations.

The effect of EDE clearly shows up at later epochs, having its maximum difference ∼ 2 per cent at $z = 0$ compared to ΛCDM. The upcoming DESI[5] and *Euclid*[6] experiments with sub-per cent accuracy on the acoustic scale measurements will be able to test models such as the EDE one considered in this work. It is interesting to note that ΛCDM_EDE, despite having the same cosmological parameters as EDE but not the same sound horizon scale, predicts

[4]There is no real peak in the power spectrum at those wavenumbers. The peak at $k \approx 1.5\,h$ Mpc^{-1} in Fig. 3 is due to the fact that we scale the power spectrum by factor $k^{5/4}$. However, there is a significant change in the slope of the power spectrum from $P(k) \propto k^{-2.5}$ in the linear regime to much flatter $P(k) \propto k^{-1.25}$.

[5]https://www.desi.lbl.gov

[6]https://sci.esa.int/web/Euclid

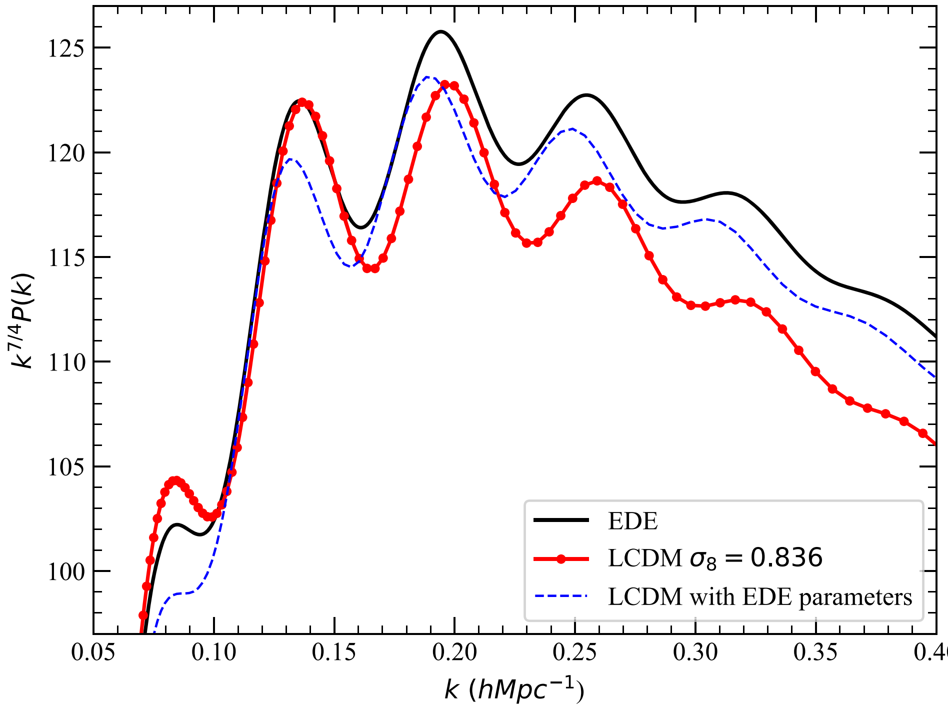

Figure 4. Linear power spectra, scaled with a factor $k^{7/4}$, for the EDE (the solid line) and ΛCDM (the dot-solid line) models in the BAO domain. A third ΛCDM model with the same cosmological parameters as EDE but without the early dark matter component is also shown (the dashed line). All models were normalized to have the same $\sigma_8 = 0.836$ to appreciate clearly the overall shape and acoustic oscillation features differences.

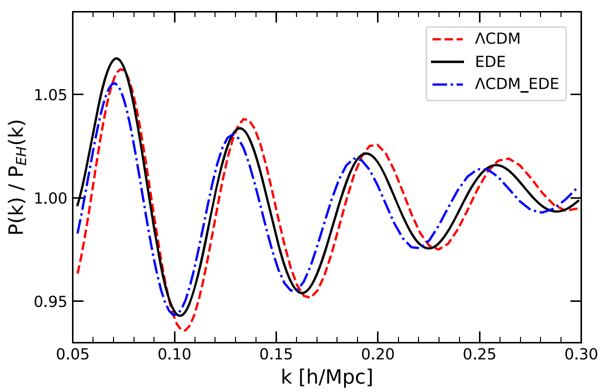

Figure 5. BAO wiggles in the linear power spectrum for the three cosmological models: EDE (the solid line), ΛCDM (the dashed line), and ΛCDM_EDE (the dot-solid line) with the same cosmological parameters as EDE. The plot shows the deviations of the power spectra from that without baryonic oscillations (Eisenstein & Hu 1998). Compared with ΛCDM, the BAO peaks in EDE are systematically shifted by 1.8 per cent to smaller wavenumbers, and in the case of ΛCDM_EDE by 4.4 per cent to smaller wavenumbers.

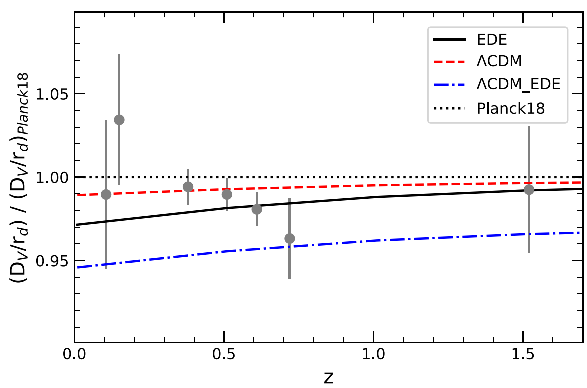

Figure 6. Acoustic-scale distance measurements relative to the prediction from *Planck* TT, TE, EE + low E + lensing in the base-ΛCDM model (see Table 1; Planck Collaboration VI 2018). The symbols and 1σ error bars correspond, in increasing redshift order, to the isotropic BAO measurements $D_V(z)/r_d$ from the 6dFGRS (Beutler et al. 2011), the SDSS-MGC (Ross et al. 2015), BOSS DR12 LRGs (at $z = 0.38$, 0.51, and 0.61, Alam et al. 2017), eBOSS DR14 LRGs (Bautista et al. 2018) and eBOSS DR14 QSOs (Ata et al. 2018). The curves provide the model predictions from EDE (solid), MultiDark-ΛCDM (dashed), and ΛCDM with the same EDE cosmological parameters (dash–dotted).

α that differs substantially at all redshifts by about 4 per cent; see Fig. 6).

The acoustic-scale distance measurements up to $z = 1.5$ displayed in Fig. 6 include density-field reconstruction of the BAO feature, which is used to partially reverse the effects of non-linear growth of structure formation (see Anderson et al. 2012; Padmanabhan et al. 2012). The shape of the linear matter power spectrum $P(k)$ is distorted by the non-linear evolution of density fluctuations, redshift distortions, and galaxy bias even at large scales $k < 0.2\ h\ \mathrm{Mpc}^{-1}$. As mentioned above, the shift parameter α yields the relative position of the acoustic scale in the power spectrum (or two-point correlation function) obtained from the data (or simulations) with respect to the adopted $P(k)$ model.

Here, we study the non-linear shift and damping of acoustic oscillations up to redshift $z = 4$ for dark matter in our ensemble of

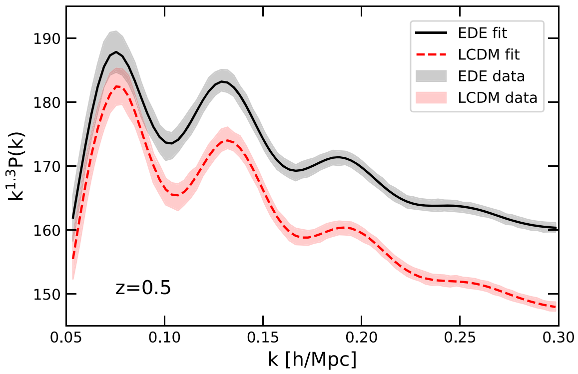

Figure 7. Mean, and standard deviation, of the dark matter power spectra at $z = 0.5$ obtained from the ensemble of ~200 EDE and ΛCDM GLAM simulations. The solid (dashed) lines correspond to the best-fitting model given by equation (2) in the wavenumber range $0.05 < k < 0.3\,\mathrm{h\,Mpc^{-1}}$ for the EDE (ΛCDM) data.

~200 EDE and ΛCDM GLAM $N-$ body simulations. Fig. 7 shows the spherically averaged power spectra at $z = 0.5$ in real-space drawn for both cosmologies in the domain of the BAO features. We measure the shift of the BAO relative to linear theory by following a similar methodology as that presented in Seo et al. (2008), and implemented in Anderson et al. (2014) to measure the BAO stretch parameter in the BOSS data. The non-linear dark matter power spectrum with wiggles is modelled by damping the acoustic oscillation features of the linear power spectrum assuming a Gaussian with a scale parameter $\Sigma_{\rm nl}$ that accounts for the BAO broadening due to non-linear effects (e.g. Eisenstein et al. 2007). We use the functional form:

$$P(k) = P_{\rm sm}(k)\left[1 + \left(\frac{P_{\rm lin}(k/\alpha)}{P_{\rm nw}(k/\alpha)} - 1\right) \mathrm{e}^{-\frac{1}{2}(k/\alpha)^2\Sigma_{\rm nl}^2}\right], \quad (2)$$

where $P_{\rm lin}$ is the linear power spectrum generated with CAMB for each cosmology model, and $P_{\rm sm}$ is the smooth ‘BAO-free’ power spectrum modelled as $P_{\rm sm} = P_{\rm nw}(k) + A(k)$ with $P_{\rm nw}(k)$ being the ‘de-wiggled’ (Eisenstein & Hu 1998) spectrum template and $A(k)$ accounting for the non-linear growth of the broad-band matter power spectrum expressed in the form of simple power-law polynomial terms $A(k) = a_1k + a_2 + A_3/k + A_4/k^2 + A_5/k^3$ (Anderson et al. 2014). The shift and damping of the acoustic oscillations, measured by α and $\Sigma_{\rm nl}$, are considered free parameters in our model.

We then perform the fit of the power spectrum $P(k)$ drawn from each of our GLAM simulations over the wavenumber range $0.05 < k < 0.3\,\mathrm{h\,Mpc^{-1}}$ for several redshifts. The solid (dashed) line in Fig. 7 corresponds to the best-fitting power spectrum model given using equation (2) for the EDE (ΛCDM) simulation data. The shift and damping of the BAO features in both cosmologies is similar as can be seen from the plot. The mean values, and 1σ uncertainties, of the α and $\Sigma_{\rm nl}$ parameters obtained from the best-fitting to each of the EDE and ΛCDM GLAM power spectra are provided in Table 3 up to $z = 4$. The non-linear damping estimated from perturbation theory[7] for each cosmology is also listed, and shows a remarkable agreement better than 2 per cent over all redshifts with that measured from our model fits to the simulation data.

[7]The broadening and attenuation of the BAO feature is exponential, as adopted in our model given in equation (2), with a scale $\Sigma_{\rm nl}^{\rm th}$ computed following Crocce & Scoccimarro (2006), Matsubara (2008), i.e. $\Sigma_{\rm nl}^{\rm th} = \left[\frac{1}{3\pi^2}\int P_{\rm lin}(k)\mathrm{d}k\right]^{1/2}$.

Our shift results for the acoustic scale towards larger k, relative to the linear power spectrum, and damping values obtained from our analysis are in good agreement with previous works for ΛCDM (e.g. Crocce & Scoccimarro 2008; Seo et al. 2010; Prada et al. 2016). Fig. 8 demonstrates that the non-linear evolution of the BAO shift (bottom panel) and damping (top panel) for the isotropic dark matter power spectrum in both EDE and ΛCDM cosmologies display small differences, with the BAO features being less affected by the non-linear growth of structure formation. Moreover, Bernal et al. (2020) shows that the ΛCDM-assumed templates used for anisotropic-BAO analyses can be used in EDE models as well.

A summary of our BAO results can also be shown in configuration space. In Fig. 9, we see that the BAO peak in the EDE linear correlation function (right-hand panel) is slightly shifted by ~ 2 per cent to larger radii compared with the ΛCDM model, as expected from their different values of the sound horizon scale at the drag epoch. The impact of non-linear evolution broadens the BAO peaks but it does not reduce the shift differences between EDE and ΛCDM.

5 HALO ABUNDANCES

To study halo mass functions, we use simulations with $500\,h^{-1}$ Mpc and $1000\,h^{-1}$ Mpc boxes and mesh size $N_{\rm g} = 7000$. Simulations with larger $2\,h^{-1}$ Gpc boxes have lower mass and force resolutions – not sufficient for analysis of galaxy-mass halo abundances.

Haloes in simulations were identified with the SO halofinder BDM (Klypin et al. 2011; Knebe et al. 2011) that uses the virial overdensity definition of Bryan & Norman (1998). The resolution was not sufficient for identifying subhaloes, so only distinct haloes are studied.

Fig. 10 shows the halo mass function at different redshifts. The EDE model predicts more haloes at any redshift, but the difference is very small at $z = 0$: a 10 per cent effect for very massive clusters $M \approx 10^{15}\,h^{-1}\,\mathrm{M_\odot}$ and just 1 per cent for Milky Way mass haloes with $M = 10^{12}\,h^{-1}\,\mathrm{M_\odot}$. These differences hardly make any impact on predicted statistics of galaxies and clusters with observational uncertainties and theoretical inaccuracies being larger than differences in halo abundances.

The situation is different at larger redshifts: the number of haloes in EDE is *substantially* larger than in ΛCDM. For example, the EDE model predicts about 50 per cent more massive clusters of mass $M = (3-5)\times 10^{14}\,h^{-1}\,\mathrm{M_\odot}$ at $z = 1$. The differences increase even more at larger redshifts. For example, the EDE model predicts almost twice more galaxy-size haloes with $M > 3\times 10^{12}\,h^{-1}\,\mathrm{M_\odot}$ at redshift $z = 4$. These are interesting predictions that can potentially be tested by comparing with abundances of high redshift $z \gtrsim 1$ clusters of galaxies (e.g. Bayliss et al. 2014; Gonzalez et al. 2015; Bocquet et al. 2019), abundances of massive galaxies and black holes at $z > 4$ (e.g. Haiman & Loeb 2001; Stefanon et al. 2015; Behroozi & Silk 2018; Carnall et al. 2020), and clustering of high-redshift galaxies (Harikane et al. 2016, 2018; Endsley et al. 2020).

Another consequence of the increased mass function in EDE is earlier collapse times. More haloes in EDE at higher redshifts implies that haloes of a given mass M form earlier in the EDE model. Because the Universe is denser at those times, so are the haloes. At later times, the accretion of dark matter on to the halo gradually builds the outer halo regions resulting in increasing halo concentration (e.g. Bullock et al. 2001). Thus, denser central regions in EDE models should lead to more concentrated haloes.

At first sight, our results on the halo mass functions are puzzling. Halo mass functions are defined by the amplitude of perturbations $\sigma(M, z)$. However, the normalization of the perturbations σ_8 is just

Table 3. Mean values of the BAO shift and damping at different redshifts obtained from the best-fitting α and $\Sigma_{\rm nl}$ parameters of the ~200 realizations of EDE$_{2B}$ and ΛCDM$_{2B}$ real-space power spectra (see Table 2). The damping computed from linear theory Σ_{nl}^{th} for each cosmology is also listed for comparison.

		ΛCDM			EDE	
Redshift	$\alpha-1$(per cent)	$\Sigma_{\rm nl}$ (Mpc h^{-1})	$\Sigma_{\rm nl}^{\rm th}$	$\alpha-1$(per cent)	$\Sigma_{\rm nl}$ (Mpc h^{-1})	$\Sigma_{\rm nl}^{\rm th}$
4.079	0.061 ± 0.020	2.089 ± 0.052	2.101	0.060 ± 0.019	2.090 ± 0.055	2.170
2.934	0.080 ± 0.022	2.745 ± 0.039	2.703	0.078 ± 0.020	2.787 ± 0.042	2.791
1.940	0.115 ± 0.024	3.650 ± 0.032	3.584	0.110 ± 0.023	3.729 ± 0.033	3.699
1.799	0.123 ± 0.024	3.823 ± 0.031	3.756	0.117 ± 0.023	3.907 ± 0.032	3.876
1.553	0.139 ± 0.025	4.162 ± 0.030	4.095	0.132 ± 0.024	4.255 ± 0.031	4.224
1.256	0.165 ± 0.027	4.650 ± 0.029	4.589	0.154 ± 0.027	4.755 ± 0.030	4.731
1.021	0.182 ± 0.026	5.095 ± 0.026	5.063	0.176 ± 0.029	5.228 ± 0.030	5.215
0.775	0.228 ± 0.032	5.688 ± 0.029	5.656	0.205 ± 0.032	5.813 ± 0.030	5.820
0.500	0.280 ± 0.036	6.456 ± 0.030	6.465	0.247 ± 0.036	6.591 ± 0.031	6.641
0.244	0.345 ± 0.042	7.306 ± 0.033	7.377	0.297 ± 0.042	7.450 ± 0.034	7.560
0.007	0.390 ± 0.043	8.184 ± 0.033	8.354	0.352 ± 0.049	8.343 ± 0.037	8.536

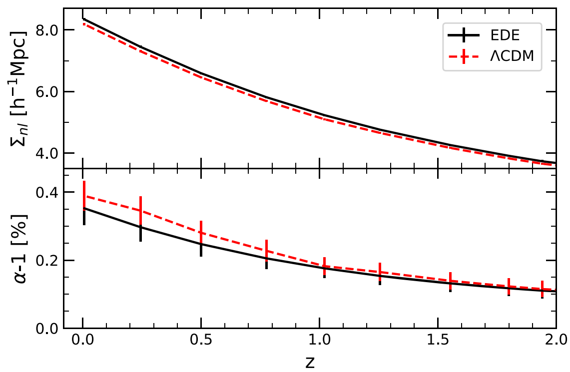

Figure 8. Non-linear evolution of the BAO shift (bottom panel) and damping (top panel) for the isotropic dark matter power spectrum in our EDE$_{2B}$ and ΛCDM$_{2B}$ simulations. The displayed mean values, and 1σ uncertainties, of α and $\Sigma_{\rm nl}$, and given in Table 6, are estimated from the ensemble of individual shifts and damping parameters measured from fitting each of the power spectra, using equation (2), of the EDE and ΛCDM GLAM simulations.

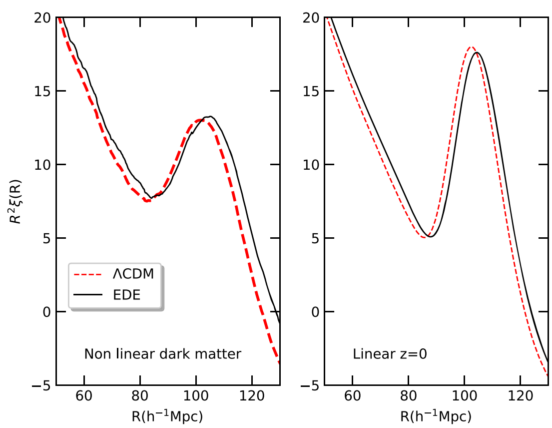

Figure 9. *Right-hand panel:* Linear correlation function of dark matter at $z=0$ on large scales. We plot the correlation function $\xi(R)$ scaled with R^2 to remove the main trend of the correlation function. The correlation function in the EDE model is slightly shifted by ~ 2 per cent to larger radii as compered with the ΛCDM model. *Left-hand panel:* Non-linear correlation function at $z=0$. Compared to the linear $\xi(R)$, the BAO peak in the non-linear regime slightly shifts to smaller values and becomes wider with smaller amplitude – effects that are well known and well understood. Non-linear effects do not reduce differences between EDE and ΛCDM models.

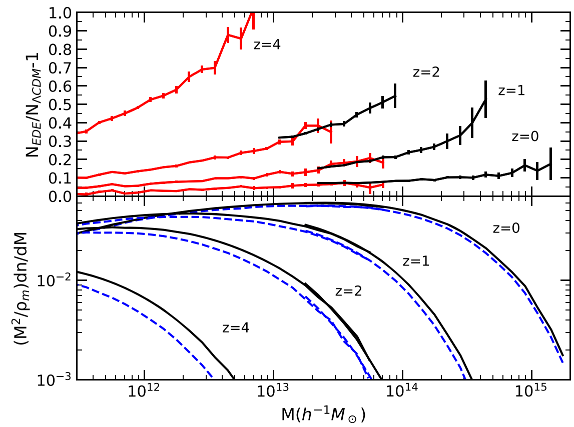

Figure 10. Halo mass function at redshifts $z=0$–4. The ull curves in the bottom panel are for the EDE simulations and the dashed curves are for the ΛCDM simulations. The smaller box and better resolution simulations EDE$_{0.5}$ and ΛCDM$_{0.5}$ are used for masses below $M \lesssim 10^{14}\,h^{-1}$ Mpc. They are shown as the red curves in the top panel. Larger box and lower resolution simulations EDE$_{2A}$ and ΛCDM$_{2A}$ (the black curves in the top panel) are used for massive haloes with $M \gtrsim 2\times10^{13}\,h^{-1}$ Mpc. At $z=0$ halo abundances are very similar for the models: EDE predicts ~ 10 per cent more of the most massive clusters $M \approx 10^{15}\,h^{-1}\,{\rm M}_\odot$ and 1–2 per cent more of galaxy-size haloes with $M \approx 10^{12-13}\,h^{-1}\,{\rm M}_\odot$. The differences in abundances increase substantially with the redshift.

2 per cent different in the EDE model. Why do we see large deviations in the halo abundances? The evolution of the mass function is defined by the growth rate of fluctuations, which in turn is defined by Ω_m, which is nearly the same for EDE and ΛCDM models. In this case why do we see large evolution of the differences between the models? In order to have some insights on the issue, we use analytical estimates of the halo mass function that allow us to change parameters and see their effects.

Specifically, we use the Despali et al. (2016) approximation for virial halo mass function at different redshifts. By itself the approximation is not accurate enough to reliably measure the differences between EDE and ΛCDM models. However, it is good enough to study trends and to probe effects of different parameters.

According to the theory (e.g. Bond et al. 1991; Sheth & Tormen 1999), the halo mass function $n(M, z)$ is a function of $\sigma(M, z)$ – the *rms* of the linear density field smoothed with the top-hat filter of radius R_{f} corresponding to the average mass M inside a sphere of radius R_{f}: $M = (4\pi/3)\rho_m R_{\mathrm{f}}^3$. Spherical fluctuations that in the linear approximation exceed a density threshold $\delta_{\mathrm{cr}} \approx 1.68$ in the real non-linear regime collapse and form dark matter haloes. The halo mass function

$$\frac{\mathrm{d}n}{\mathrm{d}M} = f(\sigma)\left[\frac{\Omega_m \rho_{\mathrm{crit}}}{M^2}\right]\frac{\mathrm{d}\ln\sigma}{\mathrm{d}\ln M} \tag{3}$$

can be written in a form that depends mostly on one parameter – the relative height of the density peak ν defined as

$$\nu = \frac{\delta_{\mathrm{cr}}}{\sigma(M,z)}. \tag{4}$$

There are different approximations for function $f(\sigma)$. We start with the Press–Schechter approximation because it is easy to see the main factors defining the mass function:

$$\left(\frac{M^2}{\Omega_m \rho_{\mathrm{crit}}}\right)\frac{\mathrm{d}n}{\mathrm{d}M} = \sqrt{\frac{2}{\pi}}\,\nu \exp\left(-\frac{\nu^2}{2}\right)\frac{\mathrm{d}\ln\sigma}{\mathrm{d}\ln M}. \tag{5}$$

When ν is small ($\nu \lesssim 1$), the Gaussian term is close to unity, and the amplitude of the mass functions is linearly proportional to ν, which, in turn, is inversely proportional to the normalization σ_8. This explains why the EDE mass function is just $\sim$ 1–2 per cent larger than in ΛCDM at small M and at $z = 0$: we are dealing with small ν peaks of the Gaussian density field. As mass increases, the *rms* of fluctuations $\sigma(M)$ decreases, and eventually ν becomes large. In this case the Gaussian term dominates, and we expect a steep decline of dn/dM. In this regime the ratio of mass functions is equal to $\approx\exp(\alpha\nu^2)$, where $\alpha = (\sigma_{8,\mathrm{EDE}}/\sigma_{8,\Lambda\mathrm{CDM}}) - 1 \approx 0.02$. For example, for 4σ fluctuations $\nu = 4$, we expect a $\sim$ 40 per cent difference. In other words, for high-ν peaks a small change in the amplitude of fluctuations produces a very large change in the halo abundance. This is exactly what we see in Fig. 10 at large redshifts.

In practice, we use a better approximation for the halo mass function provided by Despali et al. (2016). We find that the approximation is very accurate at low redshifts with the errors less than $\lesssim$ 3 per cent for masses $M_h > 10^{12}\,h^{-1}\,\mathrm{M}_\odot$. However, the errors increase with the redshift, becoming $\approx$ 12 per cent at $z = 4$ for the ΛCDM model. The errors also depend on cosmology: at $z = 4$ the error for the EDE model is $\approx$ 30 per cent. While not very accurate, the approximation can be used for qualitative analysis.

We are mostly interested in effects of modification of the amplitude σ_8 and in changes of the slope of the spectrum $P(k)$. For the base model we use ΛCDM with $\sigma_8 = 0.820$. We start with increasing the amplitude to the same value $\sigma_8 = 0.836$ as in the EDE model. When doing this, we take the same shape of spectrum as in ΛCDM and increase the normalization. The dotted curves in Fig. 11 show how the mass function changes due to the increased σ_8. As expected, the high-σ_8 model has more haloes and the difference increases with mass and with the redshift. However, the shape of the mass function ratios is too steep compared with the N-body simulations. Compare, for example, the $z = 0$ curves in Figs 10 and 11. Also, the magnitude of the effect is much smaller at $z = 4$ compared with what it should be.

Now we also change the slope of the power spectrum from $n_{\mathrm{s}} = 0.965$ to the same value $n_{\mathrm{s}} = 0.985$ as in the EDE model while keeping the same high normalization σ_8. Because the radius $R_{\mathrm{f}} = 8\,h^{-1}$ Mpc of the top-hat filter in the σ_8 definition was chosen such that the abundance of massive clusters with $M \approx 10^{15}\,h^{-1}\,\mathrm{M}_\odot$ should stay approximately constant, keeping the same σ_8 means that cluster abundance does not change much. At the same time, a steeper slope of $P(k)$ means that the amplitude of fluctuations increases for small

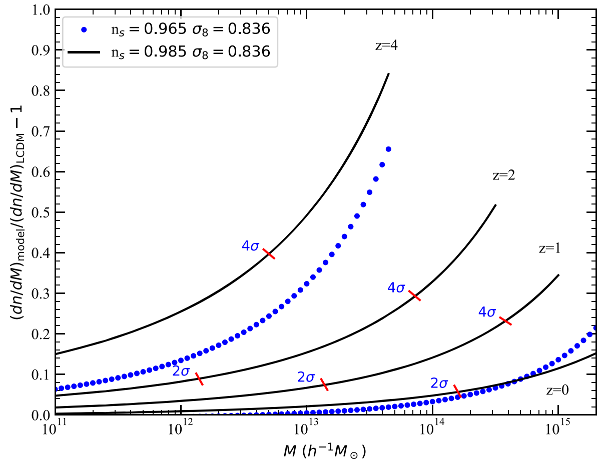

Figure 11. Analytical estimates of the ratio of halo abundances of different models relative to the abundance in the ΛCDM model. The Despali et al. (2016) approximation is used to make the predictions. The dotted curves for $z = 0$ and $z = 4$ show effects due to the increase of just normalization from $\sigma_8 = 0.820$ in ΛCDM to $\sigma_8 = 0.836$ (as in the EDE model). The full curves are for the model with increased slope $n_{\mathrm{s}} = 0.985$ (compared to $n_{\mathrm{s}} = 0.965$ in ΛCDM) and the increased $\sigma_8 = 0.836$. The small lines mark positions of peaks of given ν height. As expected, the curves start to go up steeply when haloes become high peaks of the Gaussian field. The analytical models qualitatively explain the main differences between the EDE and ΛCDM models, although they underpredict the magnitude of the real differences observed in Fig. 10.

haloes. As the result, the full curves for tilted and high-σ_8 models in Fig. 11 are flatter producing more haloes with small mass.

In Fig. 11, we also mark positions of peaks of given ν height. As expected, the curves start to steeply go up when haloes become high peaks of the Gaussian field.

In summary, the EDE model predicts quite similar (1–10 per cent) halo abundance as ΛCDM at low redshifts, significantly increasing at higher redshifts. Most of the increase is due to the change $\Delta n_{\mathrm{s}} = 0.02$ in the slope of the power spectrum with the increase in σ_8 playing an additional role. These results are well understood in the framework of the theory of the halo mass function, although the analytical approximation by Despali et al. (2016) fails to reproduce the results accurately with errors up to $\sim$ 30 per cent being redshift and model dependent.

6 HALO ABUNDANCES AND CLUSTERING AT HIGH REDSHIFTS

Results discussed in the previous section show a remarkable increase with redshift in halo abundances in the EDE model (relative to the ΛCDM model). Here, we study predictions for even larger redshifts. We focus on two issues: (a) the abundance of small haloes at the epoch of recombination ($z = 6-10$) and (b) the clustering of haloes at $z = 4-6$ that are plausibly measurable with *JWST* (Endsley et al. 2020).

We make additional simulations using smaller simulation boxes of 50 and 250 h^{-1} Mpc with 2000^3 particles and force resolutions of 7 and 36 h^{-1} kpc correpondingly, which is substantially better than in the $EDE_{0.5}$ and $\Lambda\mathrm{CDM}_{0.5}$ simulations. In addition to our EDE and ΛCDM models, we also run a simulation $\Lambda\mathrm{CDM}_{\mathrm{low}}$ with the same parameters as the ΛCDM model but with lower amplitude of fluctuations $\sigma_8 = 0.75$ that is motivated by weak-lensing results (e.g.

Hamana et al. 2020). Because of the smaller box size, the improved mass resolution of these simulations ($m_p = 1.3 \times 10^6\, h^{-1}\,\mathrm{M}_\odot$ and $m_p = 1.6 \times 10^8\, h^{-1}\,\mathrm{M}_\odot$) allows us to study halo abundances and halo clustering for haloes with masses as low as $\sim 10^9$–$10^{10}\, h^{-1}\,\mathrm{M}_\odot$.

The abundance and clustering of such low-mass haloes is particularly relevant for understanding reionization. The Universe was re-ionized between $z = 6$ and 10 (e.g. Madau & Dickinson 2014), and it is generally accepted that the observed population of relatively bright star-forming galaxies ($M_{\rm UV} < -17$; $M_h > 10^{10}\, h^{-1}\,\mathrm{M}_\odot$) cannot provide enough ionizing photons (Paardekooper, Khochfar & Dalla Vecchia 2015; Robertson et al. 2015; Finkelstein et al. 2019). However, fluxes from fainter galaxies may be sufficient (Robertson et al. 2015; Yung et al. 2020). The predicted ionizing flux of UV radiation depends on three factors: efficiency of star formation (especially in low-mass haloes), abundance of haloes of different masses at the epoch of re-ionization, and the escape fraction of photons. Theoretical estimates (Finkelstein et al. 2019; Yung et al. 2020) indicate that about 50–60 per cent of ionizing photons were produced by (but not necessarily escaped from) galaxies hosted in haloes with masses $M_h = 10^{10}$–$10^{12}\, h^{-1}\,\mathrm{M}_\odot$. These estimates are based on halo abundances in the standard ΛCDM model. Most of the radiation came from galaxies hosted by haloes with mass $M_h > 10^9\, h^{-1}\,\mathrm{M}_\odot$ (Barkana & Loeb 2001; Finkelstein et al. 2019).

We find that the trend of increasing halo abundance ratios persists during the epoch of re-ionization at redshifts $z = 6-10$. For example, at $z = 7.5$ the EDE model predicts 1.8 times more haloes with masses larger than $M = 10^{10}\, h^{-1}\,\mathrm{M}_\odot$ compared with ΛCDM. The difference with $\Lambda\mathrm{CDM_{low}}$ is even more striking: there are more than 3.7 times more haloes above that mass cut in the EDE compared with the $\Lambda\mathrm{CDM_{low}}$ model. At $z = 10$, the $\Lambda\mathrm{CDM_{low}}$ model has 8.3 times fewer haloes with $M > 5 \times 10^9\, h^{-1}\,\mathrm{M}_\odot$ compared with the EDE model.

Thus, with other parameters fixed, the EDE model would predict a factor of $\sim$1.5–2 larger ionizing fluxes compared with the ΛCDM model. Reducing the fluctuation amplitude to $\sigma_8 = 0.75$ would result in reduction of fluxes by a factor of 3–5 compared with ΛCDM, which would be problematic.

Clustering of high-redshift galaxies is potentially an interesting way to distinguish different cosmological models. Ground observations with the Hyper Suprime-Cam (HSC) Subaru telescope (e.g. Harikane et al. 2016, 2018) and future measurements of large samples of galaxies at $z = 4-6$ with *JWST* (Endsley et al. 2020) will bring an opportunity to combine galaxy clustering with abundances as a probe for halo masses and merging rates. Theoretical estimates indicate that the observed galaxies at those redshifts should be hosted by haloes with masses in the range $M = 10^{10}$–$10^{12}\, h^{-1}\,\mathrm{M}_\odot$ (Harikane et al. 2016, 2018; Endsley et al. 2020).

As we saw earlier, the EDE model predicts stronger dark matter clustering and larger halo abundances at high redshifts compared with the ΛCDM model. Thus, one would naively expect that haloes–and galaxies hosted by those haloes–should also be more clustered. However, our simulations show that this is not the case. Here, we use distinct haloes in the $\mathrm{EDE_{0.5}}$ and $\Lambda\mathrm{CDM_{0.5}}$ simulations to study clustering of haloes with masses $M = (2-5) \times 10^{11}\, h^{-1}\,\mathrm{M}_\odot$. Fig. 12 shows the results for haloes at $z = 6$ (top panels) and $z = 4$ (bottom panels). Note that the smallest radius plotted, $R = 1\, h^{-1}$ Mpc, is significantly larger than the virial radii of these haloes. Thus, the radii presented in the Figure are well in the domain of the two-halo term and are well resolved by the simulations.

The halo correlation functions at those redshifts and radii are nearly power laws, $\xi(R) \approx (R/R_0)^\gamma$, with slopes $\gamma \approx -1.7 - 1.9$, which is similar to the slope of Milky Way mass haloes at $z = 0$. The

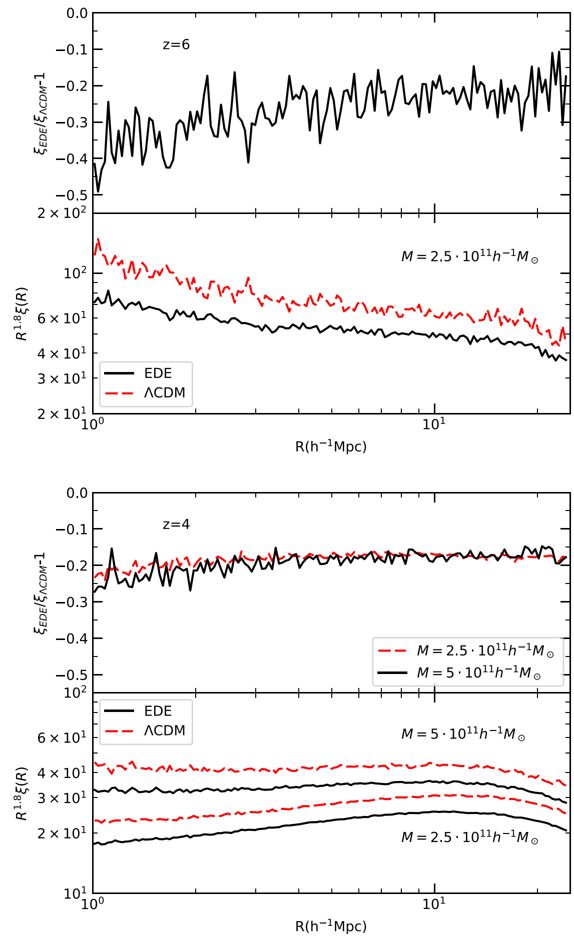

Figure 12. Correlation functions of dark matter haloes at redshift $z = 6$ (top panels) and $z = 4$ (bottom panels). Haloes above virial masses indicated in the plots were used to find the correlations and their ratios. In the distance range $R = (1–20)\, h^{-1}$ Mpc the correlation functions are well approximated by a power law $\xi(R) \propto r^{-1.8}$. At each redshift, haloes in the EDE model are less clustered by $\sim$ (10–30) per cent than haloes with the same mass cut in the ΛCDMmodel – an unexpected result considering that the dark matter in the EDE model is more clustered.

amplitudes of clustering (R_0) at high redshifts are remarkably large. For example, at $z = 6$ and $M > 2.5 \times 10^{11}\, h^{-1}\,\mathrm{M}_\odot$, the clustering scale is $R_0 = 9.9\, h^{-1}$ Mpc for ΛCDM and $R_0 = 8.8\, h^{-1}$ Mpc for the EDE model.

Somewhat unexpectedly, the clustering of haloes in the EDE model is smaller than in ΛCDM in spite of the fact that the dark matter is more strongly clustered in EDE. The differences depend on redshift and halo mass, but those dependencies are weak. Overall, at the same mass cut, haloes in EDE have correlation functions $\approx$ 20–30 per cent smaller. When we select haloes with the same cumulative number density, the differences become even smaller ($\approx$ 10 per cent). This suggests that measuring clustering at fixed galaxy number density will not be a strong test of EDE. Instead, other mass-sensitive measures (e.g. satellite kinematics or redshift-space distortions) may be more successful probes at high redshifts.

On theoretical grounds, the correlation function of dark matter haloes $\xi_{\rm hh}$ can be written as a product of two factors: $\xi_{\rm hh}(R, M) = b^2(\sigma(M))\xi_{\rm mm}(R)$, where $\xi_{\rm mm}(R)$ is the non-linear dark matter correlation function and b is the bias factor (e.g. Sheth & Tormen

1999; Sheth, Mo & Tormen 2001; Tinker et al. 2005). Note that the bias factor depends on mass only through the height of the primordial density peak $\nu = \delta_{cr}/\sigma(M, z)$. When we compare EDE and ΛCDM models at the same mass cut, we know that the bias factor b for the EDE model is *smaller* than for the ΛCDM model. The smaller b is the reason why halo abundance in EDE is larger: we are dealing with less rare and, thus, more abundant objects. As a result, the two factors in the halo mass function have the opposite tendencies: the dark matter correlation function is larger, while the bias factor is smaller. Our numerical results indicate that the bias factor has a larger effect leading to the overall decline of the halo–halo correlation function in the EDE model.

7 SUMMARY AND DISCUSSION

There are two main tensions between the standard ΛCDM cosmology and local observations, the Hubble tension and the S_8 tension. The EDE model considered here resolves the Hubble tension, which is that *Planck*-normalized ΛCDM predicts a value of the cosmological expansion rate that is smaller than local measurements by as much as 6σ. Such a large discrepancy is unlikely to be a statistical fluke. And it is probably not due to systematic errors because it is seen in different kinds of measurements, in particular Cepheid-calibrated SNe Ia giving $h = 0.674 \pm 0.006$ (Riess et al. 2019, the SH0ES team) and strong-lens time delays giving $h = 0.733 \pm 0.018$ (Wong et al. 2020, the H0LiCOW team).

As we discussed in the Introduction, this Hubble tension can be resolved by adding a maximum of 10 per cent of dark energy to the energy density of the universe for a brief period around the end of the radiation domination era at redshift $z \approx 3500$ (Smith et al. 2020, fig. 1). As we also discussed in the Introduction, this EDE model does not exacerbate the relatively small ($\sim 2\sigma$) S_8 tension in standard ΛCDM.

In this paper on the EDE model we have focused on the non-linear effects on halo abundance and clustering, including the BAOs. On large scales, the small differences between the linear power spectra of standard ΛCDM and our EDE model are mostly due to the different σ_8 values. But on smaller scales the linear theory differences become larger because of the slightly larger slope n_s of the EDE primordial power spectrum. Similar effects are expected in other EDE models that are motivated by resolving the Hubble tension (e.g. Agrawal et al. 2019; Lin et al. 2019).

In this paper, we have explored the non-linear implications of the Smith et al. (2020) EDE model using a large suite of cosmological *N*-body simulations. When non-linear effects are taken into account, standard ΛCDM and EDE differ by only about 1-10 per cent in the strongly non-linear regime $k \gtrsim 1\,h\,\mathrm{Mpc}^{-1}$ at low redshift. On the larger scales of the BAOs, in linear theory the peaks are shifted to smaller wavenumbers by about 2 per cent as a consequence of the different value of the sound horizon scale at the drag epoch. Non-linear effects broaden and damp the BAO peaks, but the $\sim$2 per cent shift to larger physical scales is robust. As Fig. 6 shows, both standard ΛCDM and the EDE model are in good agreement with all the presently available acoustic-scale distance measurements. DESI and *Euclid* measurements will soon be able to test such predictions more stringently.

The mass function of distinct dark matter haloes (those that are not subhaloes) is very similar to that of standard ΛCDM at $z = 0$, but the number of haloes in EDE becomes substantially larger at higher redshifts. An analytic analysis shows that the number of haloes increases a lot compared to ΛCDM when they correspond to fluctuations with high amplitude ν, where the Gaussian term in the mass function dominates. The increase in the number of rare cluster-mass haloes at $z \gtrsim 1$ is mainly due to the increase in σ_8 in the EDE model, while the increase in n_s causes a further increase in the number of galaxy-mass haloes at high redshift.

Our *N*-body simulations of the non-linear evolution of the EDE model show that its power spectrum and halo mass functions agree within a few per cent with those of standard ΛCDM at redshift $z = 0$, so the successful predictions of standard ΛCDM at low redshifts apply equally to the EDE cosmology. However, the EDE model predicts earlier formation of dark matter haloes and larger numbers of massive haloes at higher redshifts. This means that haloes of the same mass will tend to have higher concentrations. However, they will not have increased clustering. These predictions will be tested by upcoming observations, with all-sky cluster abundances being measured by the eROSITA X-ray satellite, and the abundance and clustering of high-redshift galaxies to be measured especially by *JWST* (e.g. Endsley et al. 2020).

Higher resolution simulations will be needed for more detailed comparisons with observations. We leave those to future work.

ACKNOWLEDGEMENTS

AK and FP thank the support of the Spanish Ministry of Science funding grant PGC2018-101931-B-I00. This work used the skun6@IAA facility managed by the Instituto de Astrofísica de Andalucía (CSIC). The equipment was funded by the Spanish Ministry of Science EU-FEDER infrastructure grant EQC2018-004366-P. MK acknowledges the support of NSF Grant No. 1519353, NASA NNX17AK38G, and the Simons Foundation. TLS acknowledges support from NASA (through grant 80NSSC18K0728) and the Research Corporation. We thank Alexie Leauthaud and Johannes Lange for a helpful discussion about weak lensing results.

DATA AVAILABILITY

Data used in this paper (detailed code description, power spectra and halo catalogs) are available on https://www.skiesanduniverses.org Klypin, Prada, Comparat (2017).

REFERENCES

Abbott T. M. C. et al., 2019, Phys. Rev. D, 100, 023541
Agrawal P., Cyr-Racine F.-Y., Pinner D., Randall L., 2019, preprint (arXiv:1904.01016)
Alam S. et al., 2017, MNRAS, 470, 2617
Anderson L. et al., 2012, MNRAS, 427, 3435
Anderson L. et al., 2014, MNRAS, 441, 24
Angulo R. E., Baugh C. M., Frenk C. S., Lacey C. G., 2008, MNRAS, 383, 755
Angulo R. E., Pontzen A., 2016, MNRAS, 462, L1
Ata M. et al., 2018, MNRAS, 473, 4773
Aubourg É. et al., 2015, Phys. Rev. D, 92, 123516
Aylor K., Joy M., Knox L., Millea M., Raghunathan S., Kimmy Wu W. L., 2019, ApJ, 874, 4
Barkana R., Loeb A., 2001, Phys. Rep., 349, 125
Bartelmann M., Doran M., Wetterich C., 2006, A&A, 454, 27
Baugh C. M. et al., 2019, MNRAS, 483, 4922
Bautista J. E. et al., 2018, ApJ, 863, 110
Bayliss M. B. et al., 2014, ApJ, 794, 12
Behroozi P., Silk J., 2018, MNRAS, 477, 5382
Bernal J. L., Smith T. L., Boddy K. K., Kamionkowski M., 2020, Phys. Rev. D., 102, 123515
Bernal J. L., Verde L., Riess A. G., 2016, J. Cosmol. Astropart. Phys., 2016, 019

Beutler F. et al., 2011, MNRAS, 416, 3017
Bianchini F., et al., 2020, ApJ, 888, 119
Bocquet S. et al., 2019, ApJ, 878, 55
Bond J. R., Cole S., Efstathiou G., Kaiser N., 1991, ApJ, 379, 440
Bryan G. L., Norman M. L., 1998, ApJ, 495, 80
Bullock J. S., Kolatt T. S., Sigad Y., Somerville R. S., Kravtsov A. V., Klypin A. A., Primack J. R., Dekel A., 2001, MNRAS, 321, 559
Carnall A. C. et al., 2020, MNRAS, 496, 695
Chudaykin A., Gorbunov D., Nedelko N., 2021, Phys. Rev. D., 103, 043529
Crocce M., Scoccimarro R., 2006, Phys. Rev. D, 73, 063520
Crocce M., Scoccimarro R., 2008, Phys. Rev. D, 77, 023533
Despali G., Giocoli C., Angulo R. E., Tormen G., Sheth R. K., Baso G., Moscardini L., 2016, MNRAS, 456, 2486
Dodelson S., Kaplinghat M., Stewart E., 2000, Phys. Rev. Lett., 85, 5276
Doran M., Lilley M., Schwindt J., Wetterich C., 2001, ApJ, 559, 501
D'Amico G., Senatore L., Zhang P., Zheng H., 2020, preprint (arXiv:2006.12420)
Eisenstein D. J., Hu W., 1998, ApJ, 496, 605
Eisenstein D. J., Seo H.-J., White M., 2007, ApJ, 664, 660
Eisenstein D. J. et al., 2005, ApJ, 633, 560
Endsley R., Behroozi P., Stark D. P., Williams C. C., Robertson B. E., Rieke M., Gottlöber S., Yepes G., 2020, MNRAS, 493, 1178
Finkelstein S. L. et al., 2019, ApJ, 879, 36
Fontanot F., Springel V., Angulo R. E., Henriques B., 2012, MNRAS, 426, 2335
Francis M. J., Lewis G. F., Linder E. V., 2009, MNRAS, 394, 605
Freedman W. L., 2017, Nature Astronomy, 1, 121
Gonzalez A. H. et al., 2015, ApJ, 812, L40
Griest K., 2002, Phys. Rev. D, 66, 123501
Grossi M., Springel V., 2009, MNRAS, 394, 1559
Guo H. et al., 2015, MNRAS, 453, 4368
Haiman Z., Loeb A., 2001, ApJ, 552, 459
Hamana T. et al., 2020, PASJ, 72, 16
Harikane Y. et al., 2016, ApJ, 821, 123
Harikane Y. et al., 2018, PASJ, 70, S11
Hernández-Aguayo C., Prada F., Baugh C. M., Klypin A., 2021, MNRAS, 503, 2318
Hikage C. et al., 2019, PASJ, 71, 43
Hill J. C., McDonough E., Toomey M. W., Alexander S., 2020, Phys. Rev. D., 102, 043507
Ishiyama T., Enoki M., Kobayashi M. A. R., Makiya R., Nagashima M., Oogi T., 2015, PASJ, 67, 61
Ishiyama T. et al., 2020, preprint (arXiv:2007.14720)
Ivanov M. M., McDonough E., Hill J. C., Simonović M., Toomey M. W., Alexander S., Zaldarriaga M., 2020, Phys. Rev. D, 102, 103502
Jedamzik K., Pogosian L., Zhao G.-B., 2020, preprint (arXiv:2010.04158)
Kamionkowski M., Pradler J., Walker D. G. E., 2014, Phys. Rev. Lett., 113, 251302
Karwal T., Kamionkowski M., 2016, Phys. Rev. D, 94, 103523
Kitaura F.-S. et al., 2016, MNRAS, 456, 4156
Klypin A., Prada F., 2018, MNRAS, 478, 4602
Klypin A., Prada F., Byun J., 2020, MNRAS, 496, 3862
Klypin A., Prada F., Comparat J., 2017, preprint (arXiv:2017.1711.01453)
Klypin A., Yepes G., Gottlöber S., Prada F., Heß S., 2016, MNRAS, 457, 4340
Klypin A. A., Trujillo-Gomez S., Primack J., 2011, ApJ, 740, 102
Knebe A. et al., 2011, MNRAS, 415, 2293
Knox L., Millea M., 2020, Phys. Rev. D, 101, 043533
Kravtsov A. V., Klypin A. A., Khokhlov A. M., 1997, ApJS, 111, 73
Lin M.-X., Benevento G., Hu W., Raveri M., 2019, Phys. Rev. D, 100, 063542
Madau P., Dickinson M., 2014, ARA&A, 52, 415
Matsubara T., 2008, Phys. Rev. D, 77, 063530
Merloni A. et al., 2012, preprint (arXiv:1209.3114)
Murgia R., Abellán G. F., Poulin V., Phys. Rev. D., 2020, 103, 063502
Müller C. M., Schäfer G., Wetterich C., 2004, Phys. Rev. D, 70, 083504
Paardekooper J.-P., Khochfar S., Dalla Vecchia C., 2015, MNRAS, 451, 2544
Padmanabhan N., Xu X., Eisenstein D. J., Scalzo R., Cuesta A. J., Mehta K. T., Kazin E., 2012, MNRAS, 427, 2132
Planck Collaboration VI, 2018, A&A , 641, A6
Planck Collaboration XVI, 2014, A&A, 571, A16
Poulin V., Smith T. L., Grin D., Karwal T., Kamionkowski M., 2018, Phys. Rev. D, 98, 083525
Poulin V., Smith T. L., Karwal T., Kamionkowski M., 2019, Phys. Rev. Lett., 122, 221301
Prada F., Scóccola C. G., Chuang C.-H., Yepes G., Klypin A. A., Kitaura F.-S., Gottlöber S., Zhao C., 2016, MNRAS, 458, 613
Riess A. G., Casertano S., Yuan W., Macri L. M., Scolnic D., 2019a, ApJ, 876, 85
Robertson B. E., Ellis R. S., Furlanetto S. R., Dunlop J. S., 2015, ApJ, 802, L19
Rodríguez-Puebla A., Behroozi P., Primack J., Klypin A., Lee C., Hellinger D., 2016, MNRAS, 462, 893
Rodríguez-Torres S. A. et al., 2016, MNRAS, 460, 1173
Ross A. J., Samushia L., Howlett C., Percival W. J., Burden A., Manera M., 2015, MNRAS, 449, 835
Seo H.-J., Siegel E. R., Eisenstein D. J., White M., 2008, ApJ, 686, 13
Seo H.-J. et al., 2010, ApJ, 720, 1650
Sheth R. K., Mo H. J., Tormen G., 2001, MNRAS, 323, 1
Sheth R. K., Tormen G., 1999, MNRAS, 308, 119
Smith T. L., Poulin V., Amin M. A., 2020, Phys. Rev. D, 101, 063523
Smith T. L., Poulin V., Bernal J. L., Boddy K. K., Kamionkowski M., Murgia R., 2020, preprint (arXiv:2009.10740)
Springel V., 2005, MNRAS, 364, 1105
Stefanon M. et al., 2015, ApJ, 803, 11
Tinker J. L., Weinberg D. H., Zheng Z., Zehavi I., 2005, ApJ, 631, 41
Troxel M. A. et al., 2018, Phys. Rev. D, 98, 043528
Verde L., Treu T., Riess A. G., 2019, Nat. Astron., 3, 891
Villaescusa-Navarro F. et al., 2020, ApJS, 250, 2
Wong K. C. et al., 2020, MNRAS, 498, 1420
Yung L. Y. A., Somerville R. S., Finkelstein S. L., Popping G., Davé R., Venkatesan A., Behroozi P., Ferguson H. C., 2020, MNRAS 496, 4574

APPENDIX A: COMPARISON OF GLAM RESULTS WITH THOSE OF DIFFERENT SIMULATIONS AND CODES

The GLAM code has already been extensively tested and compared with other high-resolution simulations in Klypin & Prada (2018). In particular, fig. 2 in Klypin & Prada (2018) presents detailed comparison of power spectra of GLAM simulations with those of the MultiDark simulations (Klypin et al. 2016) that were performed with the GADGET code (Springel 2005). In Hernández-Aguayo et al. (2021), we compare halo mass functions and correlation functions of GLAM and the *Planck* Millennium simulation (Baugh et al. 2019) again made with the GADGET code. Here, we present more tests.

We start with comparing our results on the power spectrum with the power spectra of the QUIJOTE simulations (Villaescusa-Navarro et al. 2020). The latter used cosmological parameters $\Omega_{\rm m} = 0.3173$, $\Omega_{\rm b} = 0.049$, $n_{\rm s} = 0.9624$, $\sigma_8 = 0.834$, $h = 0.671$. The simulations were done for 512^3 particles moving in the computational box $1\,h^{-1}$ Gpc. In total there were 15 000 realizations. We use the same cosmological parameters as the QUIJOTE simulations in our GLAM runs. We make two sets of simulations. One set has large box size of $2\,h^{-1}$ Gpc and relatively low resolution of $1\,h^{-1}$ Mpc. It is designed to study the accuracy of the code at very long waves. The other set of simulations has smaller box of $1\,h^{-1}$ Gpc and much better force resolution of $0.167\,h^{-1}$ Mpc. It is to study small scales. In total we produced 90 new realizations.

To reduce effects of cosmic variance, we make simulations in pairs. In each pair phases of fluctuations are rotated by 180°. This is done by making one 'normal' random realization. For second realization of the pair we change the sign of initial perturbations of the gravitational potential. This dramatically reduces the cosmic

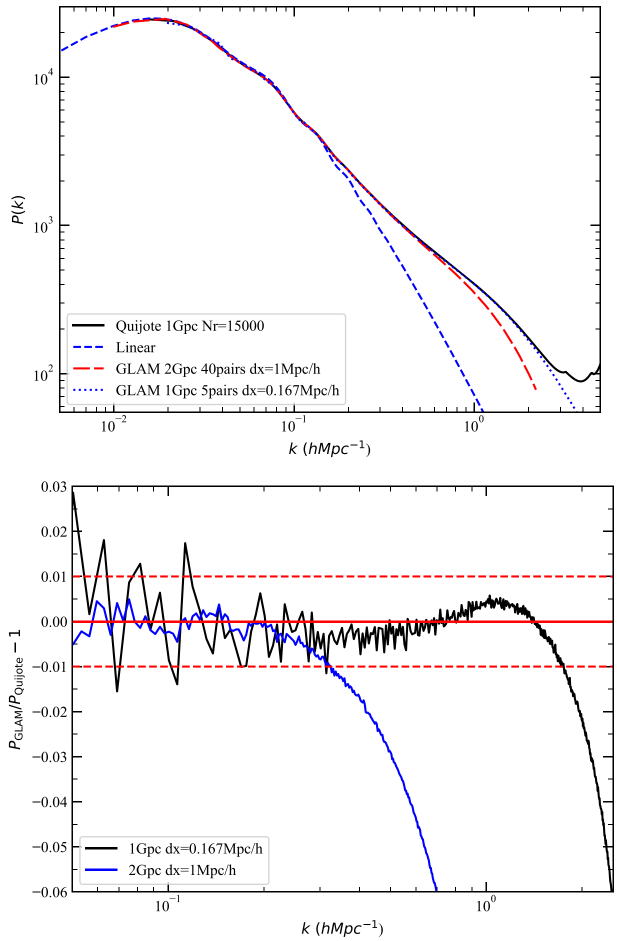

Figure A1. Comparison of power spectra of QUIJOTE and GLAM simulations at $z = 0$. The top panel shows power spectra for a wide range of wavenumbers. Note that $P(k)$ for Quijote simulations stops declining at $k \sim 3\,h$ Mpc^{-1} due to uncertain aliasing and shot noise corrections. The true spectrum must decline at those wavenumbers. The bottom panel focuses on the BAO domain and shows relative errors.

variance on long quasi-linear scales without biasing the sample. For more details, see Angulo & Pontzen (2016) and Klypin, Prada & Byun (2020).

Fig. A1 presents power spectra of QUIJOTE and GLAM simulations. Because of small cosmic variance in $2\,h^{-1}$ Gpc GLAM and QUIJOTE simulations, relative errors are less than ~ 0.3 per cent at $k < 0.2\,h$ Mpc^{-1}. GLAM simulations with $1\,h^{-1}$ Gpc boxes have errors less than ~ 0.5 per cent for $k = (0.3 - 1.5)\,h$ Mpc^{-1}. Steep decline of curves at $k > 0.3\,h$ Mpc^{-1} for $2\,h^{-1}$ Gpc simulations and at $k > 2\,h$ Mpc^{-1} are due to limited force resolutions in GLAM simulations.

The wavenumber $k_{1\ \rm per\ cent}$ at which the GLAM power spectra fall 1 per cent below the QUIJOTE simulations scales linearly with the force resolution $\Delta x = Box/N_{\rm g}$. We can combine results for the QUIJOTE simulations with those presented by Klypin & Prada (2018; fig. 2) for the MultiDark simulations to find dependence of $k_{1\ \rm per\ cent}$ on the force resolution: $k_{1\ \rm per\ cent} = (0.25 \pm 0.05)/\Delta x$, where Δx is in units h^{-1} Mpc. If we apply this estimate to EDE$_0$.5 and ΛCDM$_0$.5 simulations for which $\Delta x = 71\,h^{-1}$ kpc, we find that GLAM power spectra have errors less than 1 per cent for $k < 3.5\,h$ Mpc^{-1}.

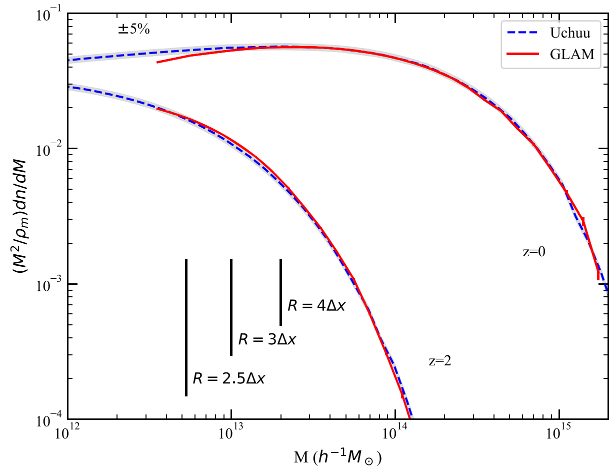

Figure A2. Mass function of distinct haloes in Uchuu and GLAM simulations with the same cosmological parameters and halo definition. The vertical lines show masses for haloes that have specified halo radii in units of cell size $\Delta x = 143\,h^{-1}$ kpc indicated in the plot. The larger the radius the better is force resolution and more accurate is the halo mass. The shaded areas show ± 5 per cent deviations from the Uchuu mass functions. Halo mass function of GLAM simulations become accurate with errors less than 5 per cent for masses $M > 5 \times 10^{12}\,h^{-1}\,{\rm M}_\odot$ corresponding to haloes resolved with 2.5–3 resolution elements Δx along the virial radius.

In order to test the accuracy of the halo mass function, we compare results of GLAM simulations with those of the 2.1 trillion particles high-resolution simulation Uchuu (Ishiyama et al. 2020), which was done using a $2\,h^{-1}$ Gpc box size with massively parallel TREEPM code GREEM (Ishiyama et al. 2015). We use the same cosmological parameters and the same halo definition (spherical ‘virial’ overdensity) as in Uchuu. Parameters of these GLAM simulations are the same as for EDE$_1$ simulations: $1\,h^{-1}$ Gpc box, 8 billion particles, 7000^3 mesh (force resolution $143\,h^{-1}$ kpc). We made 15 realizations to reduce effects of the cosmic variance.

Fig. A2 presents results of (distinct) halo mass functions at $z = 0$ and $z = 2$. Halo mass function of GLAM simulations become accurate (errors less than 5 per cent) for masses $M > 5 \times 10^{12}\,h^{-1}\,{\rm M}_\odot$ corresponding to >500 dark matter particles. However, for the GLAM code a better measure of the accuracy is the force resolution: a halo must be resolved with at least a few resolution elements to produce reasonable estimates. For the GLAM code, we find that one needs 2.5−3 elements per virial radius to achieve errors less than ~ 5 per cent.

This paper has been typeset from a TEX/LATEX file prepared by the author.